Supporting Information

Molecular-Level Precursor Engineering Enables High Utilization of Closed Nanopores in Hard Carbon for Sodium-Ion Batteries

Rui Li[a,1], *Beilei Yuan*[b,1], *Yupeng Feng*[a], *Yuhan Li*[a], *Na Jiang*[a], *Ping Liu*[b], *Liangzhi Li*[b], *Weiyue Li*[b], *Chunwei Dong*[c*], *Shuchun Hu*[d], *Qi Liu*[a], *Jian Chen*[b*], *Fei Li*[e*], *Jianping Long*[a*], *Anjun Hu*[a*]

[a] College of Materials and Chemistry & Chemical Engineering (College of Lithium Resources and Lithium Battery Industry), Chengdu University of Technology, Chengdu 610059, China

[b] Department of Materials Science and Engineering, Sichuan University of Science and Engineering, Zigong 643000, China

[c] National Institute of Clean-and-Low-Carbon Energy, Future Science & Technology City, Changping District, Beijing 102209, China.

[d] School of Electronic Engineering, Chengdu Technological University, Chengdu, 611730, China

[e] School of Materials and Energy, University of Electronic Science and Technology of China, Chengdu 611731, China

[1] These authors contributed equally to this work.

[*] Corresponding authors: 20066669@chnenergy.com.cn; jchenzg@aliyun.com (Jian Chen); feili@uestc.edu.cn; longjianping@cdut.cn (Jianping Long); anjunhu@cdut.edu.cn (Anjun Hu)

Experimental

Materials synthesis (Anode)

Natural bamboo (Phyllostachys pubescens) harvested from Sichuan Province, China, was used as the raw material. The bamboo was dried at 80 °C for 24 h, then crushed and passed through a 300-mesh sieve to obtain uniform bamboo powder with a particle size of no more than 48 μm. All chemical reagents were used as received without further purification, including sodium acetate (CH_3COONa, ≥99.0%, Aladdin), hydrofluoric acid (HF, 40 wt%, Sinopharm Chemical Reagent Co.), polyvinylidene fluoride (PVDF, HSV 900, Arkema), carbon black (Super P, TIMCAL), and N-methyl-2-pyrrolidone (NMP, ≥99.5%, Aladdin). Deionized water with a resistivity of at least 18.2 MΩ·cm was used throughout the experiments. For systematic comparison, three types of HC materials were prepared in this study: i) Pre-SA-BHC (sodium acetate-treated sample): 50 g of bamboo powder was stirred with 450 mL of 1 mol L^{-1} sodium acetate solution at 80 °C for 2 h, then transferred to a high-pressure reactor for hydrothermal treatment at 300 °C for 10 h to obtain the precursor. ii) Pre-H-BHC (hydrothermal control sample): The preparation procedure was the same as that for SA-BHC, except that the sodium acetate solution was replaced with an equal volume of deionized water. iii) Pre-D-BHC (direct pyrolysis control sample): 50 g of bamboo powder was pre-carbonized under an argon atmosphere by heating at 2 °C min^{-1} to 300 °C and holding for 2 h to obtain the precursor. All precursors were immersed in 5 wt% HF solution for 12 h to remove inorganic impurities, followed by washing with deionized water until neutral (pH ≈7) and drying at 80 °C for 10 h. Finally, the purified Pre-D-BHC, Pre-H-BHC and Pre-SA-BHC were placed in a tube furnace and heated at a rate of 2 °C min^{-1} to 1300 °C under argon protection for 2 h to undergo high-temperature carbonization. The resulting final hard carbon materials were named D-BHC, H-BHC and SA-BHC respectively.

Materials synthesis (Cathode)

The $NaNi_{0.3}Mn_{0.4}Fe_{0.1}Co_{0.1}Ti_{0.1}O_2$ (NNTMFCO) cathode material was prepared via a conventional solid-state reaction method. First, stoichiometric amounts of NiO, MnO_2, Fe_2O_3, Co_2O_3, and TiO_2 powders were weighed, with an additional 3 mol% Na_2CO_3 added to compensate for sodium volatilization during high-temperature processing. The raw materials were uniformly mixed in acetone by ball milling (rotation speed: 350 rpm, duration: 10 h). The mixed powder was then pressed into pellets and calcined at 900 ℃ for 12 h in air. Finally, the obtained product was stored in an argon-filled glove box ($H_2O < 0.1$ ppm, $O_2 < 0.1$ ppm) to avoid moisture absorption and oxidation.

Materials characterization

The crystal structure evolution and surface functional groups of the synthesized materials were systematically characterized by X-ray diffraction (XRD; Bruker D8), Raman spectroscopy (LABRAM-1B, 473 nm laser), and Fourier-transform infrared spectroscopy (FTIR; Bruker Tensor 27). Thermogravimetric analysis (TGA) was employed to investigate the pyrolysis behavior. The micromorphology, microcrystalline structure, and elemental distribution were examined using high-resolution transmission electron microscopy (HRTEM) coupled with energy-dispersive X-ray spectroscopy (EDS). Chemical composition of the electrode materials was analyzed by X-ray photoelectron spectroscopy (XPS). The specific surface area, pore volume, and pore size distribution of the samples were determined from N_2 adsorption-desorption isotherms at 77 K and CO_2 adsorption at 273 K, measured on a Micromeritics ASAP 2460 analyzer. Closed-pore characteristics were evaluated using a small-angle X-ray scattering (SAXS) system (Nano-inXider, Xenocs, France). True density was measured via helium pycnometry using an AccuPyc II 1340 analyzer. Surface potential mapping of the electrode sheets was performed with Kelvin probe force microscopy (KFM) (E-Sweep). Time-of-flight secondary ion mass spectrometry (TOF-SIMS) experiments were carried out on an ION-TOF 5-100 instrument under an analysis chamber pressure below 1.1×10^{-9} mbar. In delayed extraction mode, organic imaging was conducted using a pulsed 20 keV Bi^{3+} primary ion beam. Depth profiling was performed with a 1 keV Cs^{+} sputtering beam, with sputtering and analysis areas set to 280×280 μm^2 and 100×100 μm^2, respectively. Conductivity measurements of the hard carbon samples were carried out using a ST2742C four-probe powder conductivity tester.

Electrochemical measurements

The working electrode was prepared by mixing the synthesized HC material, Super P conductive carbon, and carboxymethyl cellulose (CMC) binder in a weight ratio of 8:1:1. The mixture was thoroughly dispersed in deionized water to form a homogeneous slurry, which was then coated onto 12 μm-thick copper foil using a doctor blade coater (MSK-AFA-200, MTI Corp.) with a gap height of 150 μm. The resulting slurry was cast uniformly onto a copper foil current collector and then dried under vacuum at 80 °C for 12 h. After drying, the electrodes were calendered with a roll press (MSK-MR100D, MTI Corp.) under a linear pressure of 5 MPa to obtain a uniform electrode density. Finally, the electrodes were punched into discs with a diameter of 12 mm. The mass loading of the active material was typically controlled at 1-1.5 mg cm^{-2}, while high-loading electrodes were prepared in the range of 2.2-2.8 mg cm^{-2}. CR2032-type coin cells were assembled in an argon-filled glove box (H_2O < 0.1 ppm, O_2 < 0.1 ppm). Sodium foil (10 mm diameter) was used as the counter/reference electrode, and the electrolyte consisted of 1 M $NaPF_6$ in diglyme (DME). A glass fiber membrane (Whatman GF/D) was employed as the separator. Based on the specific capacities of the SA-BHC anode (350 mAh g^{-1}) and the NNTMFCO cathode (120 mAh g^{-1}), pouch cells (SA-BHC||NNTMFCO) were assembled with a negative-to-positive capacity (N/P) ratio of 1.2. To better simulate practical conditions, the pouch cells used 1 M $NaPF_6$ in EC/DEC (1:1 by volume) as the electrolyte, while the separator remained identical to that in the coin cells. Electrochemical performance was tested in the voltage range of 2.0-4.2 V at various C-rates (0.1C-5C). The galvanostatic intermittent titration technique (GITT) was carried out on a Neware battery test system between 0.01 and 3.0 V at a current density of 0.05C. The procedure consisted of a 10 min charge/discharge pulse followed by a 90 min relaxation step, repeated cyclically. Charge-discharge cycling was performed using the same Neware system, while cyclic voltammetry (CV) and electrochemical impedance spectroscopy (EIS) were conducted with a CHI660E electrochemical workstation.

XRD Analysis

Crystallite dimensions were calculated using the Scherrer equation with K=0.89 and λ =0.154056 nm:

La (nm): Lateral size from the (100) peak: L_a (nm)=$K\lambda/\beta\sin\theta$, where β is the FWHM.

Lc (nm): Stacking height from the (002) peak: L_c (nm)= $K\lambda/\beta\cos\theta$, where β is the FWHM.

d (nm): Interlayer spacing was determined using Bragg's law: $d = n\lambda/2\sin\theta$, where θ is the Bragg angle and n is the reflection order (typically n=1 for the primary peak).

In-situ analysis

In situ Raman spectroscopy was performed in continuous scanning mode inside an argon-filled glovebox, utilizing an in situ electrochemical cell (provided by Hefei In-situ Technology) coupled with an electrochemical workstation to enable synchronous monitoring during charge/discharge processes. For in situ XRD analysis, a specialized X-ray transparent in situ cell was employed, with galvanostatic charge/discharge tests conducted within a voltage window of 0.01-3 V at 0.1C.

The calculation of the utilization rate of the closed pore

The theoretical volumetric capacity density of sodium metal ($C_{v,\,Na}$) is calculated by multiplying its gravimetric capacity ($C_{g,\,Na}$) by its density (ρ_{Na}):

$$C_{v,\,Na} = C_{g,\,Na} \times \rho_{Na} \qquad (1)$$

Where :

$C_{g,\,Na}$ = 1166 mAh g^{-1} is the theoretical gravimetric capacity of Na metal.

ρ_{Na} = 0.986 g cm^{-3} is the density of Na metal at room temperature.

$C_{v,\,Na}$ = 1128 mAh cm^{-3} represents the resultant theoretical volumetric capacity density.

Theoretical pore capacity:

$Q_{\text{pore-theoretial}} = V_{\text{closed pore}} \times 1128\ \text{mAh cm}^{-3}$ (2)

The closed pore utilization is calculated as:

Closed pore utilization = $Q_{\text{Plateau (0.01-0.04 V)}} / Q_{\text{pore-theoretial}}$ (3)

Supplementary calculation section

All density functional theory (DFT) calculations were performed using the Vienna Ab initio Simulation Package (VASP). The exchange-correlation interactions were treated within the generalized gradient approximation (GGA) using the Perdew-Burke-Ernzerhof (PBE) functional. The projector augmented-wave (PAW) method was employed to describe the interactions between ion cores and valence electrons. A plane-wave cutoff energy of 600 eV was adopted, and structural optimizations were conducted using a Monkhorst-Pack k-point mesh of 2 × 2 × 1. Geometry optimization was considered converged when the forces on all atoms were below 0.02 eV/Å. The average potentials (Pa) were derived from the formation energy (Ef) based on the following equations:The average potentials (P_a) were calculated based on the formation energy (E_f) according to the following formulas:

$$E_f = E_{M_xC} - xE_{M_{max}C} - (1-x)E_C \tag{4}$$

$$P_a = \frac{-[E_{M_xC} - (x-y)E_C - E_{M_yC}]}{(x-y)e} \tag{5}$$

where EMC, EC, EM and e represent the total energies of Na in the carbon matrix, carbon matrix, the Na atom in the metallic crystal form and the electron charge, respectively.

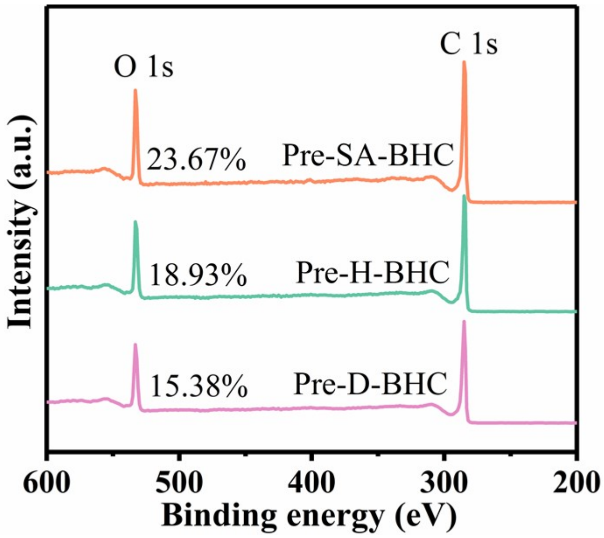

Fig. S1. XPS full spectra of Pre-SA-BHC, Pre-H-BHC, and Pre-D-BHC.

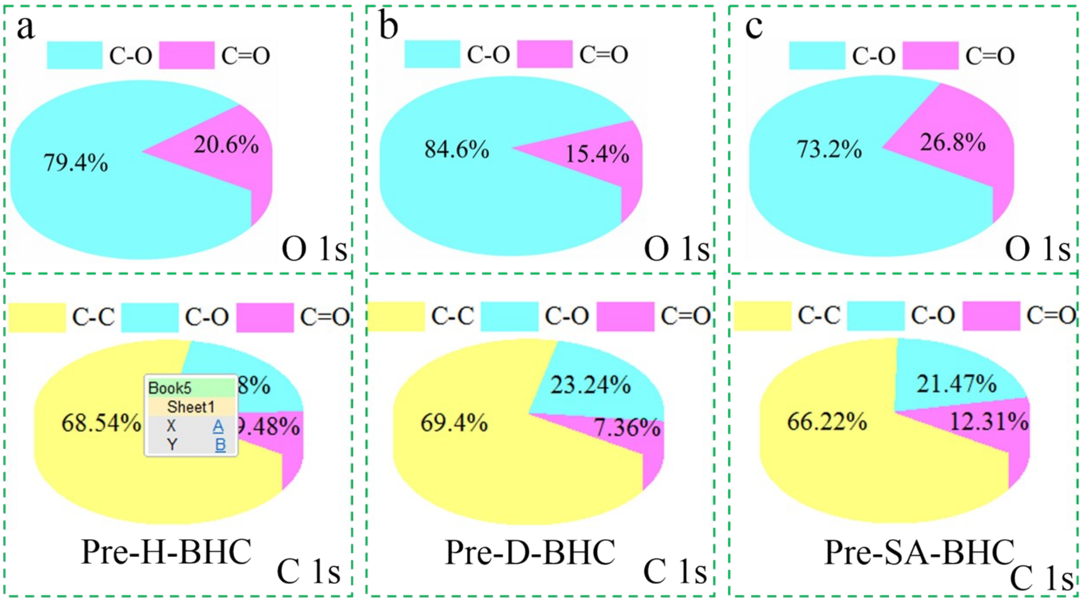

Fig. S2. The quantitative analysis results of the XPS spectra of the oxygen-containing functional groups of the Pre-H-BHC (a), Pre-D-BHC (b), and Pre-SA-BHC (c).

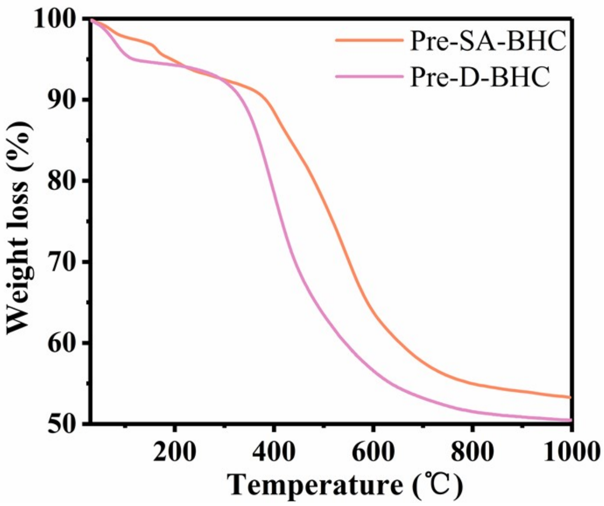

Fig. S3. TGA analyses of Pre-D-BHC and Pre-SA-BHC.

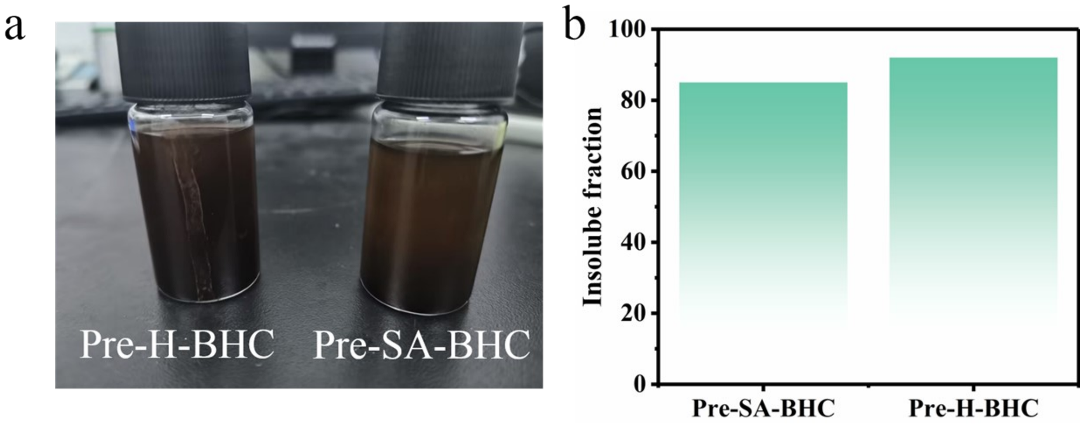

Fig. S4. (a) Photographs of Pre-SA-BHC and Pre-H-BHC after being left in ethanol for 24 h, (b) Insoluble fraction (IF) of Pre-SA-BHC and Pre-H-BHC in ethan

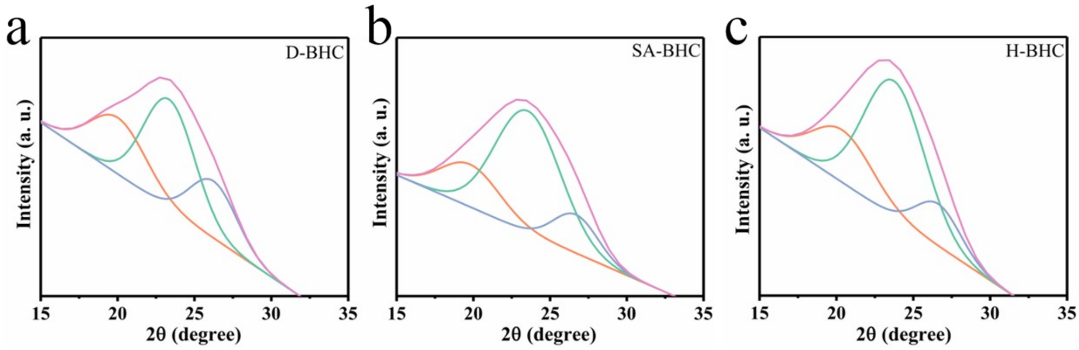

Fig. S5. (a-c) Fitted XRD patterns.

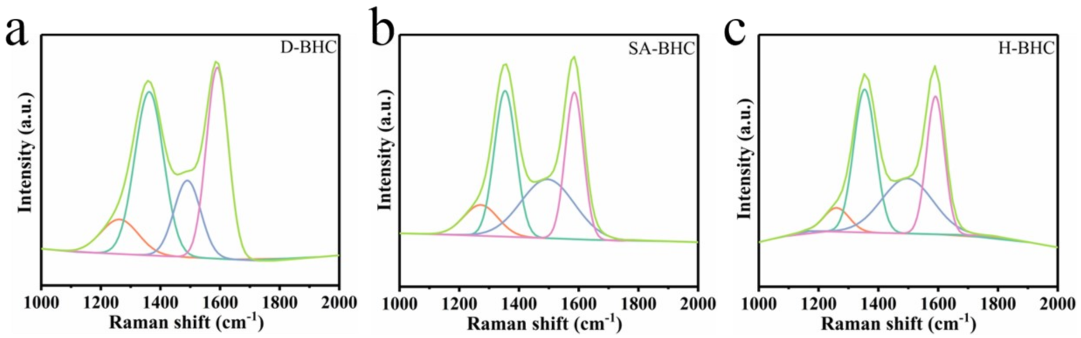

Fig. S6. (a-c) Fitted Raman patterns

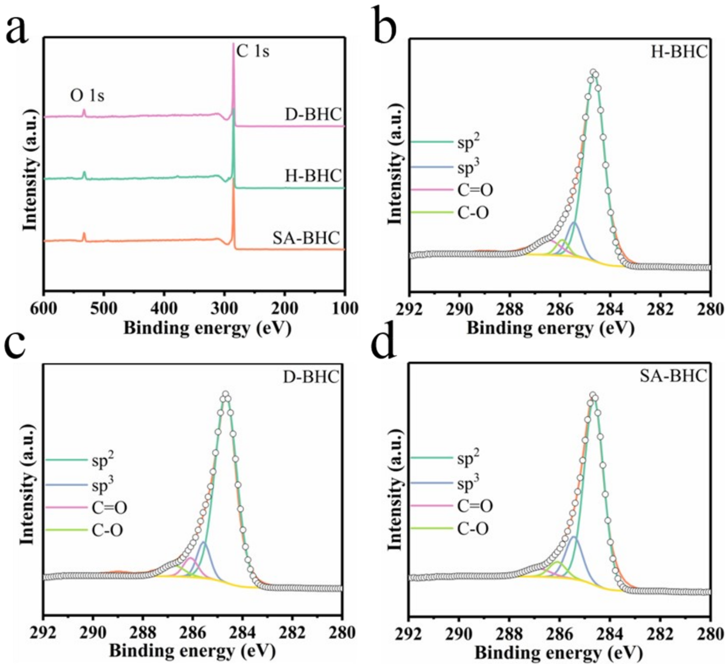

Fig. S7. XPS survey spectra for SA-BHC, H-BHC, and D-BHC. High-resolution C 1s spectra for (b) H-BHC, (c) D-BHC, (d) SA-BHC.

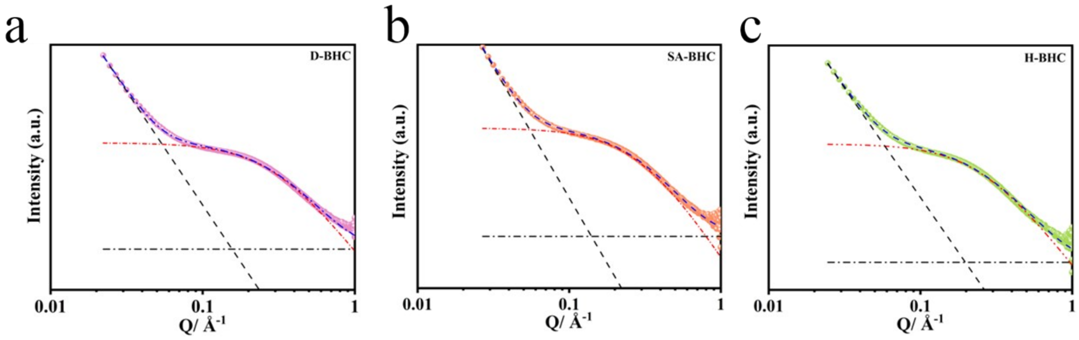

Fig. S8. The SAXS fitting curves of (a) D-BHC, (b) SA-BHC, and (c) H-BHC.

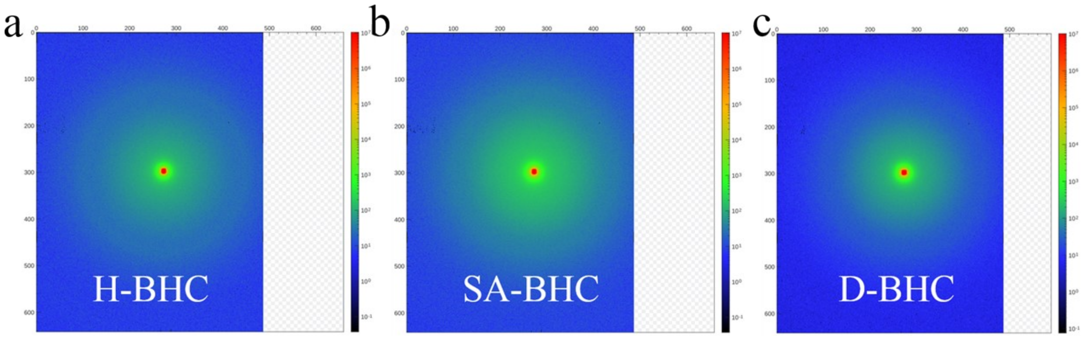

Fig. S9. SAXS 2d spectral structure of (a) H-BHC, (b) SA-BHC, and (c) D-BHC.

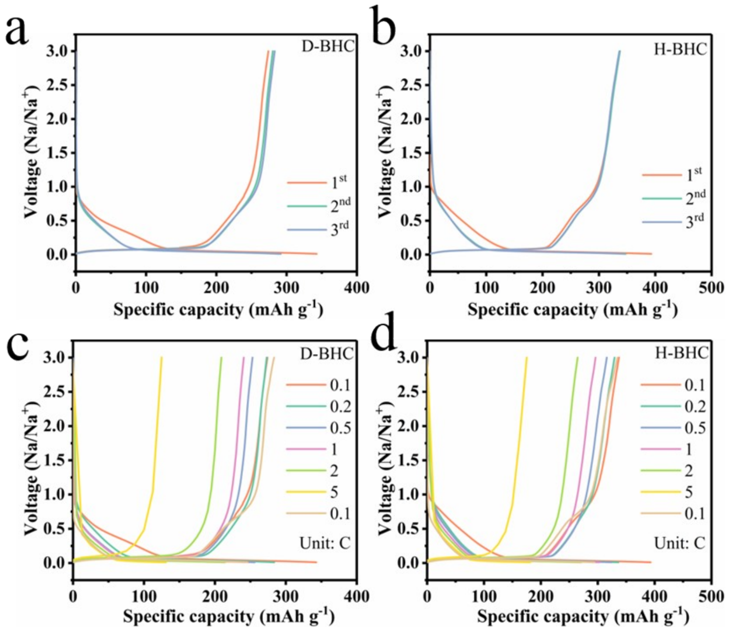

Fig. S10. GCD profiles of the a) D-BHC and b) H-BHC. d) The GCD curves of c) D-BHC and d) H-BHC at 0.1-5C.

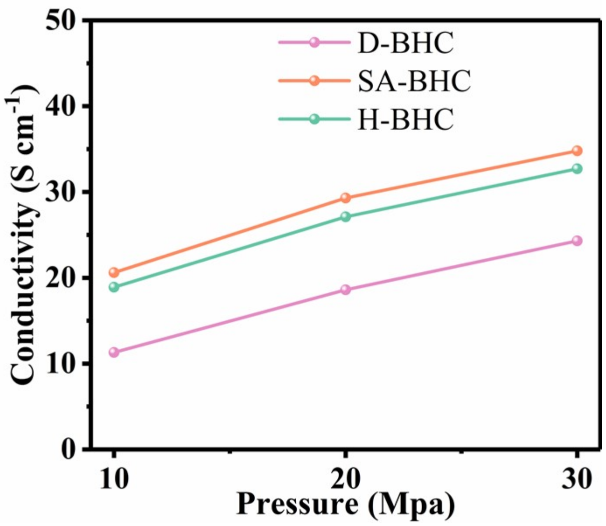

Fig. S11. Specific resistance for D-BHC, H-BHC, and SA-BHC.

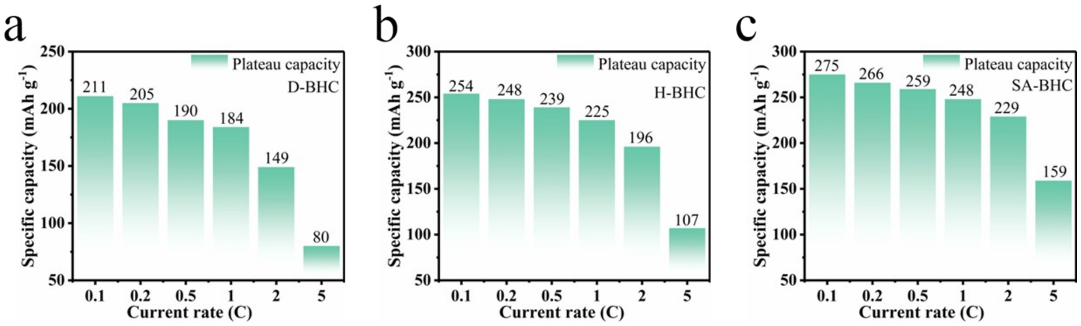

Fig. S12. Corresponding capacity contributions attributed to the plateau region and slope region.

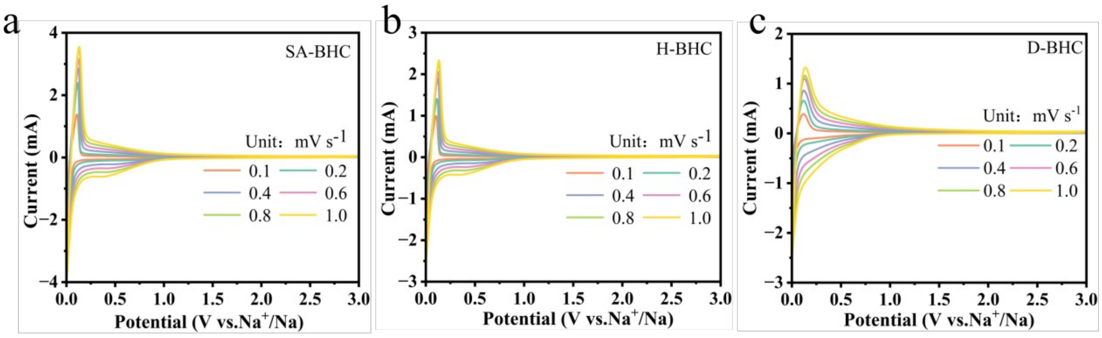

Fig. S13. CV curves at various scan rates, a) D-BHC, b) H-BHC, c) SA-BHC.

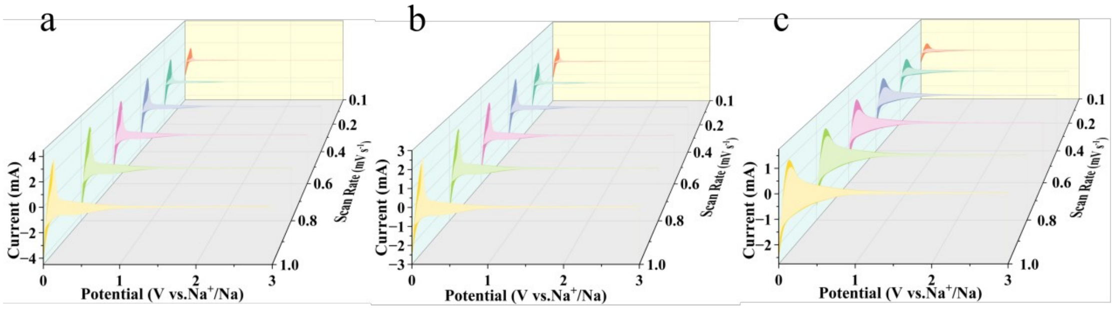

Fig. S14. Capacitive charge-storage contributions of a) D-BHC, b) H-BHC, and c) SA-BHC at different scan rates from 0.1 to 1 mV s^{-1}.

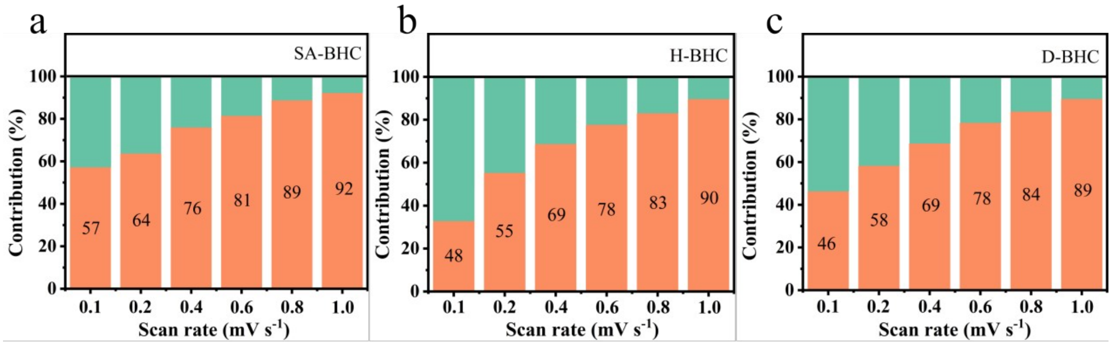

Fig. S15. Capacitive and diffusion-controlled capacity contributions for the SA-BHC, D-BHC and H-BHC electrode at different scan rates.

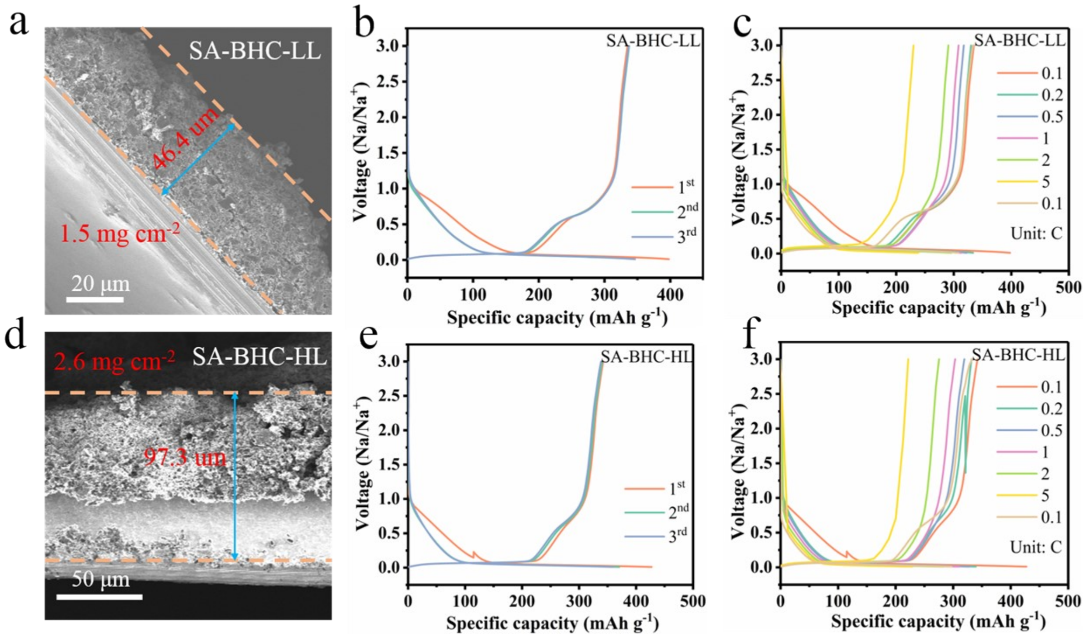

Fig. S16. Side view SEM images of a) SA-BHC-LL. b) GCD profiles of SA-BHC-LL at 0.1C. c) GCD profiles of SA-BHC-LL at 0.1-5C. Side view SEM images of d) SA-BHC-HL. e) GCD profiles of SA-BHC-HL at 0.1C. f) GCD profiles of SA-BHC-HL at 0.1-5C.

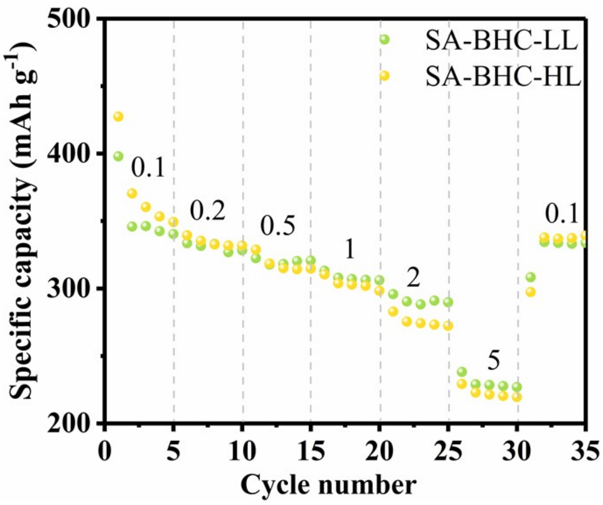

Fig. S17. Rate performances of SA-BHC-HL and SA-BHC-LL.

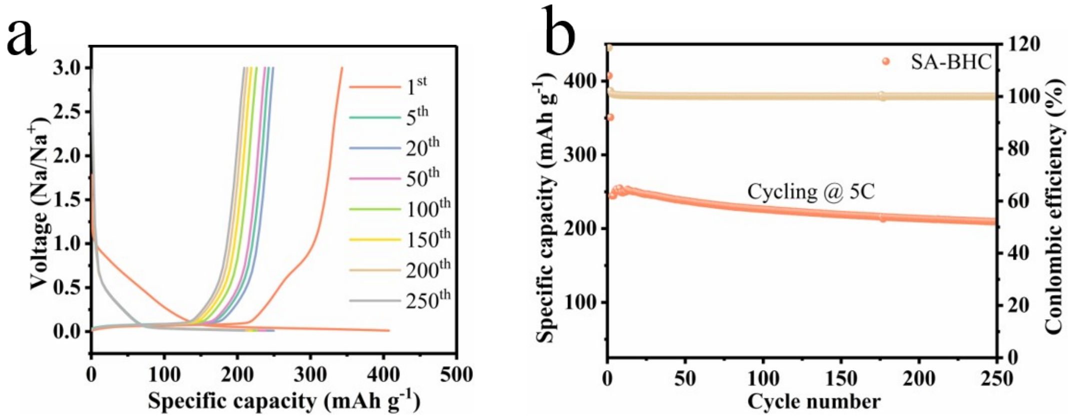

Fig. S18. a) Galvanostatic charge and discharge curves of SA-BHC at 5C. b) Cycling performance of SA-BHC at 5C.

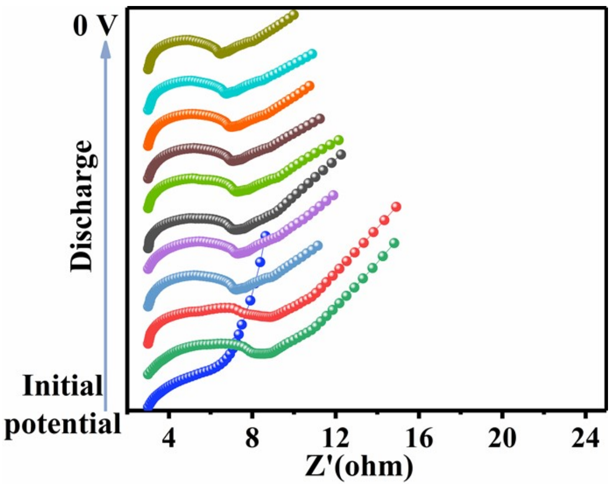

Fig. S19. *In situ* EIS curves of D-BHC during the discharge stage.

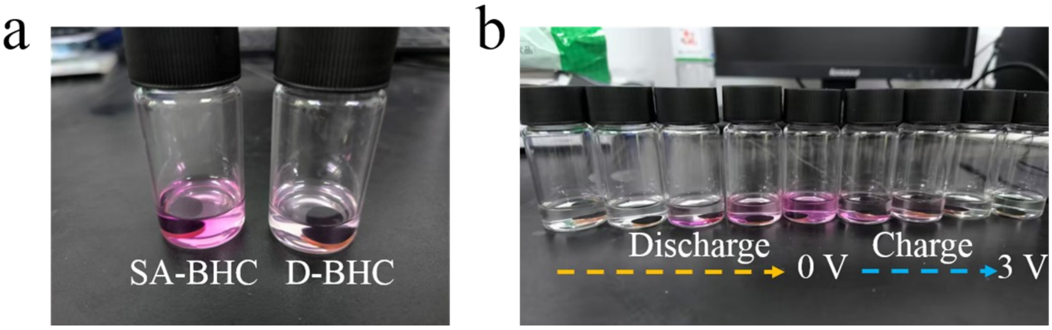

Fig. S20. (a) The color changes of ethanol containing 1% phenolphthalein after reaction with D-BHC and SA-BHC at 0.01 V. (b) Colorimetry experiment of SA-BHC electrodes at the OCP and after being discharged to 1, 0.3, 0.15, 0.04, 0.01 V and charged to 0.02, 0.04, 0.15 and 3 V in an ethanol solution containing phenolphthalein.

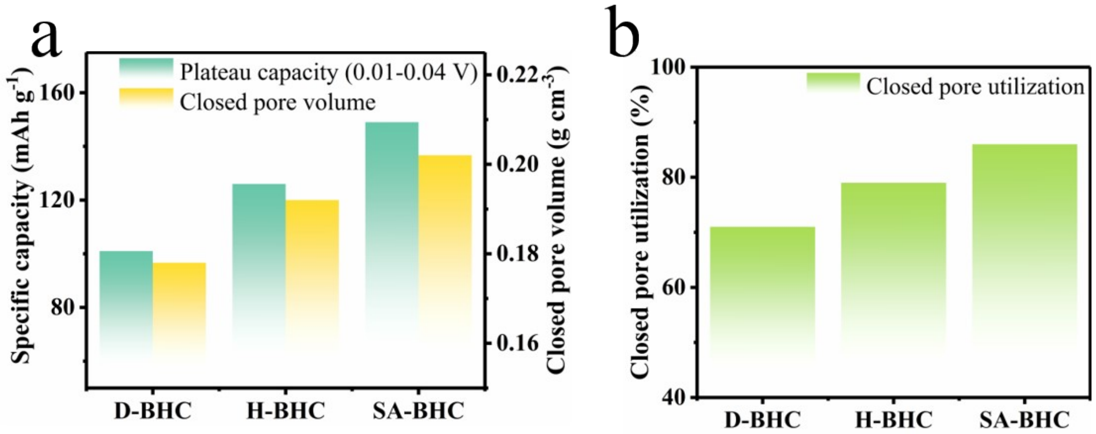

Fig. S21. a) Comparison of D-BHC, H-BHC and SA-BHC in terms of plateau capacity at 0.01-0.04 V and the volume of the closed pore for the three samples: D-BHC, H-BHC and SA-BHC. b) The closed pore utilization of the D-BHC, H-BHC and SA-BHC electrodes.

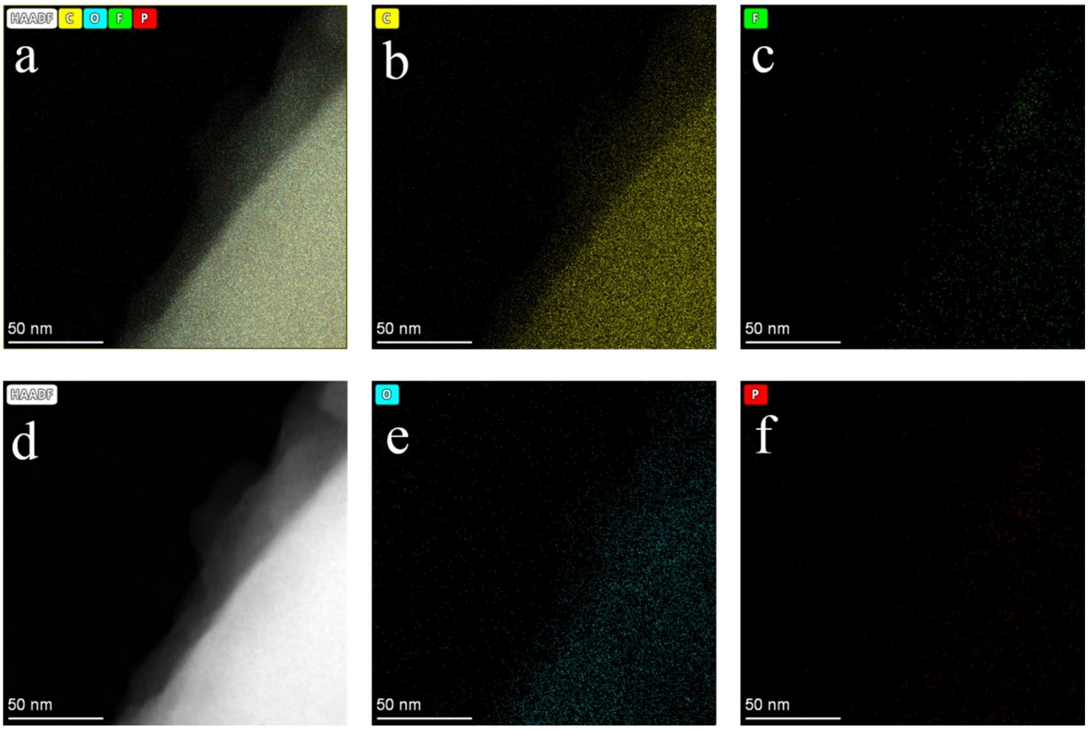

Fig. S22. (a-f) TEM mapping images of SEI of SA-BHC.

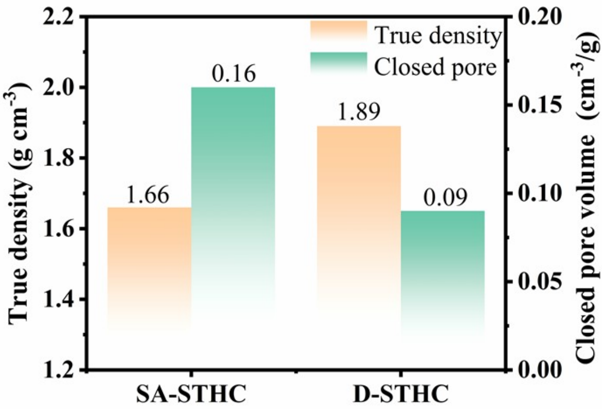

Fig. S23. The true density and closed-pore volume of D-STHC and SA-STHC.

Table S1. Physical parameters of all samples from XRD patterns.

	D-BHC	**H-BHC**	**SA-BHC**
$2\theta_{002}$ (º)	23.6	23	22.7
d_{002} (nm)	0.372	0.383	0.391
Lc (nm)	0.98	1.21	1.38
Highly disordered	28.2%	21.9%	20.8%
Pseudo-graphitic	48.2%	58.6%	65.1%
Graphite-like	23.6%	19.5%	14.1%

Table S2. Physical parameters of different hard carbons from the Raman spectra.

	A_{D1}/A_G	A_{D2}/A_G	A_{D3}/A_G	**La**
D-BHC	4.13	0.79	0.87	8.28
SA-BHC	3.25	0.89	2.04	6.36
H-BHC	2.66	0.83	0.84	7.19

Notes: D_1 band at 1350 cm^{-1} corresponds to vibrations of disordered carbon atoms from a defective graphitic structure or the edges of the graphitic sheets. The D_3 band at 1500 cm^{-1} is produced by the short-range sp^3 carbon vibration of amorphous carbon, and the D_4 band at 1200 cm^{-1} is associated with the disordered graphitic lattice or vibration of hybrid carbon of polyenes and ionic impurities at the graphene-terminated edge. A_{D1}/A_G is positively correlated with the content of graphene edge defects; A_{D3}/A_G can indicate the content of amorphous carbon and oxygen-containing functional groups.

Table S3. Pore structure parameters of HC

Samples	S_{BET} **(N_2)**	$V_{micropore}$**(N_2) (0-2 nm)**	$V_{mesoporous}$**(N_2) (2-10nm)**	V_{total}**(CO_2)**	**SAXS (Pore-pore distance)**	**True density**	V_{Closed}
Units	$m^2\ g^{-1}$	$cm^3\ g^{-1}$	$cm^3\ g^{-1}$	$cm^3\ g^{-1}$	nm	$g\ cm^{-3}$	$cm^3\ g^{-1}$
D-BHC	32.7	0.00474	0.039	0.0039	2.56	1.91	0.127
H-BHC	21.1	0.00646	0.048	0.0078	2.43	1.72	0.141
SA-BHC	24.3	0.00966	0.057	0.015	2.21	1.68	0.155

Table S4. Performance comparison of bamboo hard carbon anodes.

Precursor	**Loadings (mg cm^{-2})**	**ICE (%)**	**Capacity (mAh g^{-1})**	**Rate (mAh g^{-1}/A g^{-1})**	**Ref**
Bamboo	1.3-1.7	88.9	369.8	261.4/1.5	This work
Bamboo	1.3-1.7	84.1	348.5	295.9/0.3	[S1]
Bamboo	~2	86.8	350	83/1	[S2]
Bamboo	1.3-1.7	73.4	268.9	47.2/1.5	[S3]
Bamboo	\	81.7	338	78/0.9	[S4]
Bamboo	1	86.8	335.3	283.9/0.3	[S5]
Bamboo	0.8-1.2	82	422	318/6	[S6]
Bamboo	0.8-1.2	75	346	228/1	[S7]
Bamboo	2	68.1	280	150/0.6	[S8]
Bamboo	1.2-1.4	86.54	320	260/1	[S9]

Bamboo	\	74	346.9	187.2/1	[S10]
Bamboo	0.8-1.2	92.9	300	226/0.8	[S11]
Bamboo	1.2-1.6	90.76	348.6	201/3	[S12]

References

[S1] T. Y. Xu, X. Qiu, X. Zhang, Y. Y. Xia, *Chem. Eng. J.* 2023, 452, 139514, https://doi.org/10.1016/j.cej.2022.139514.

[S2] Y. L. Wang, Z. L. Yi, L. J. Xie, Y. X. Mao, W. J. Ji, Z. J. Liu, X. X. Wei, F. Y. Su, C. M. Chen, *Adv. Mater*. 2024, 36, 2401249, https://doi.org/10.1002/adma.202401249.

[S3] S. Pothaya, C. Poochai, N. Tammanoon, Y. Chuminjak, T. Kongthong, T. Lomas, C. Sriprachuabwong, A. Tuantranont, *Rare Metals* 2024, 43, 124-137, https://doi.org/10.1007/s12598-023-02414-w.

[S4] Y. M. Cao, X. Li, J. Peng, B. S. Chen, N. Dang, J. Zhang, J. Y. Xie, T. B. Zhao, *Langmuir* 2025, 41, 9559-9566, https://doi.org/10.1021/acs.langmuir.5c00660.

[S5] J. Kuai, J. Xie, J. D. Wang, J. Y. Chen, J. Wang, F. Liu, X. W. Xu, J. Tu, J. P. Cheng, *J. Power Sources* 2025, 627, 235792, https://doi.org/10.1016/j.jpowsour.2024.235792.

[S6] N. Lan, Y. S. Shen, J. Y. Li, H. N. He, C. H. Zhang, *Adv. Mater.* 2025, 37, 2412989, https://doi.org/10.1002/adma.202412989.

[S7] Z. Y. Huang, J. H. Huang, L. Zhong, W. L. Zhang, X. Q. Qiu, *Small* 2024, 20, 2405632, https://doi.org/10.1002/small.202405632.

[S8] Y. Leng, S. D. Dong, Z. Chen, Y. X. Sun, Q. Xu, L. X. Ma, X. He, C. X. Hai, Y. Zhou, *J. Power Sources* 2024, 613, 234826, https://doi.org/10.1016/j.jpowsour.2024.234826.

[S9] C. Wu, Y. R. Yang, Y. H. Zhang, H. Xu, W. J. Huang, X. X. He, Q. H. Chen, H. H. Dong, L. Li, X. Q. Wu, S. L. Chou, *Angew. Chem. Int. Ed.* 2024, 63, e202406889, https://doi.org/10.1002/anie.202406889.

[S10] L. M. Zhou, G. Y. Zhang, C. C. Xu, J. X. Li, Y. Y. Liu, B. J. Li, A. Wang, K. Sun, *Adv. Funct. Mater*. 2025, 35, 2416061, https://doi.org/10.1002/adfm.202416061.

[S11] Z. B. Sun, Z. R. Li, Y. J. Li, Z. H. Wang, H. F. Zuo, L. Zhao, X. G. Liu, *Chem. Eng. J.* 2025, 521, 167011, https://doi.org/10.1016/j.cej.2025.167011.

[S12] Y. F. Shen, B. J. Fan, Y. H. Xin, Q. B. Zhou, Y. S. Wang, H. Zhou, K. Y. Zhao, F. Wu, H. C. Gao, *Carbon* 2025, 243, 120594, https://doi.org/10.1016/j.carbon.2025.120594.